Aptamer Conformational Dynamics Modulate Neurotransmitter Sensing in Nanopores

Annina Stuber,[†] Ali Douaki,[‡] Julian Hengsteler,[†] Denis Buckingham,[†] Dmitry Momotenko,[¶] Denis Garoli,[*,‡] and Nako Nakatsuka[*,†]

†*Laboratory of Biosensors and Bioelectronics, Institute for Biomedical Engineering, ETH Zürich, CH-8092, Switzerland*

‡*Instituto Italiano di Tecnologia, Via Morego 30, 16163, Genova, Italy*

¶*Department of Chemistry, Carl von Ossietzky University of Oldenburg, Oldenburg D-26129,Germany*

E-mail: denis.garoli@iit.it; nakatsuka@biomed.ee.ethz.ch

Abstract

Aptamers that undergo conformational changes upon small-molecule recognition have been shown to gate the ionic flux through nanopores by rearranging charge density within the aptamer-occluded orifice. However, mechanistic insight into such systems where biomolecular interactions are confined in nanoscale spaces, is limited. To shed light on the fundamental mechanisms that facilitate the detection of small-molecule analytes inside structure-switching aptamer-modified nanopores, we correlated experimental observations to theoretical models. We developed a novel dopamine aptamer-functionalized nanopore sensor with femtomolar detection limits and compared the sensing behavior with a serotonin sensor fabricated with the same methodology. When sensing these two neurotransmitters with comparable mass and equal charge, the sensors showed an opposite electronic behavior. This distinctive phenomenon was extensively studied using complementary experimental techniques such as quartz crystal

microbalance with dissipation monitoring, in combination with theoretical assessment by the finite element method and molecular dynamic simulations. Taken together, our studies demonstrate that the sensing behavior of highly sensitive aptamer-modified nanopores correlates with the structure-switching mechanisms unique to the selected aptamers targeting specific small-molecule analytes. We believe that such investigations not only improve our understanding of the complex interactions occurring in confined nanoscale environments, but will also drive further innovations in biomimetic nanopore technologies.

Introduction

Aptamer-integrated solid-state nanopores can serve as biomimetic systems that simulate how protein channels control ionic transport selectively in response to small-molecule binding. Aptamers are artificial, single-stranded oligonucleotides isolated through an iterative evolutionary method to interact specifically with analytes of interest.[1,2] Advances in selection methodologies have enabled the discovery of aptamers targeting small molecules,[2,3] which are conventionally difficult targets with minimal available functional groups for recognition.[4–6] Coupling such selective bioreceptors inside nanoscale pores with geometries that complement and confine the aptamer-target interactions enables measurements that approach single-molecule sensitivities.[7–9] Nanoscale pores can be prepared using different strategies.[10–13] In particular, glass nanopipettes are one of the most convenient nanopore platforms due to the ease of fabrication *via* laser pulling, which can yield pore sizes ranging from a few to tens of nanometers with high reproducibility.[14,15]

Aptamer-modified nanopipette sensors can be designed based on various strategies. One relies on either partial occlusion of the nanopore through binding of large biomolecules or alterations in surface charge density due to capture of highly charged analytes.[8,16,17] An alternative, generalizable method that does not rely on the molecular properties of the analyte and thus is suitable for detection of small molecules, exploits structure-switching

aptamers that capture targets through rearrangement of their 3-D conformation.[18–20] For instance, the small molecule cocaine was hypothesized to modulate the opening and closing of aptamer-modified nanopores ∼20 nm in size.[21] Similarly, adenosine 5'-triphosphate (ATP)-aptamer-functionalized nanopores (∼10 nm) were proposed to induce open *vs.* closed states dependent on the presence/absence of ATP respectively.[22] While this work noted the synergistic effect of conformation and surface charge effects, the latter was presumed to be influenced by the capture of two negatively charged ATP molecules per aptamer.

However, it is important to consider another influence on the charge density beyond the properties of the target analyte. The rearrangement of the negatively charged aptamer backbone upon target-induced conformational change may have a greater impact on the distribution of charge inside the nanopore, especially for small-molecule targets with limited charge.[23,24] Further, characterization of the size of the aptamer in the free *vs.* target-bound state is critical to enable prediction of the conformational dynamics inside the nanopore. Previously, nanopipettes with ∼10 nm nanopores were functionalized with *ca.* 5 nm thick serotonin aptamer layers that undergoes structure switching on the order of ∼1 nm monitored by quartz crystal microbalance with dissipation monitoring (QCM-D).[25] This data led to the hypothesis that the nanopore is fully occluded with a mesh of DNA aptamers, permeable to ions and small molecules while preventing the entry of larger nonspecific species. Serotonin sensors were deployed for serotonin quantification from human neurons in complex medium without clogging.[26] Such nanoscale sensors for neurotransmitter detection facilitate localized measurements with spatial resolution that approaches synaptic dimensions.

Herein, we have developed a specific and selective dopamine aptamer-modified nanopipette sensor with femtomolar detection limits. Beyond developing highly sensitive nanoscale dopamine biosensors for neuroscience, our goal was to glean mechanistic insight into the function of small-molecule nanopore sensors driven by structure-switching. Detection of comparably sized and equally charged small molecules (serotonin and dopamine both carry a single positive charge per molecule under physiological conditions) using identical nanopore

dimensions, allowed investigations into the influence of target-specific aptamer conformational dynamics on the measured sensor response. We observed an opposite trend in the ionic current rectification behavior for the dopamine *vs.* serotonin nanopipette sensors, which indicated that the target-specific aptamer structural rearrangement was the driving mechanism for signal transduction rather than analyte charge detection.

The conformational dynamics of the dopamine aptamer was studied both experimentally and theoretically and compared with the dynamics observed in the serotonin aptamer sensor. The divergent directionality of structure switching for the dopamine *vs.* serotonin aptamers were corroborated by QCM-D results. Finally, molecular dynamics simulations (MDS), previously shown to predict oligonucleotide tertiary structures accurately,[27–31] were performed to simulate the aptamers in their free *vs.* target-bound states. Correlations between experimental and theoretical findings demonstrate the potential of MDS as a tool to predict aptamer structure-switching mechanisms. Further, values of aptamer height change extracted from the MDS enabled calculations *via* the finite element method to correlate the electrochemical behavior of the sensor to aptamer-specific conformational dynamics inside the nanopore.

Materials and Methods

Materials

Sigma-Aldrich Chemie GmbH (Buchs, Switzerland) was the main supplier for chemicals used in this work, unless otherwise noted. All measurements utilized, phosphate buffer saline (PBS) at 1x concentration (137 mM NaCl, 2.7 mM KCl, 10 mM Na_2HPO_4, 1.8 mM KH_2PO_4 and pH 7.4 (ThermoFisher Scientific AG, Reinach, Switzerland) as received. Deionized water (resistivity 18.2 MΩcm^{-1} at 25 °C produced by a Milli-Q system Millipore, Billerica, MA) was used for the preparation of all solutions. All aptamers were purchased and HPLC-purified by Microsynth AG (Balgach, Switzerland). Aptamer stock solutions of 100 μM were aliquoted

and stored at -20 °C until use. The following thiolated single-stranded DNA sequences were used in this work: *dopamine aptamer*: 5'/Thiol/CGA CGC CAG TTT GAA GGT TCG TTC GCA GGT GTG GAG TGA CGT CG/3' with molecular weight 13,871.8 g/mol and melting point 73.7 °C, and *scrambled sequence*: 5'/Thiol/ AGT ACG TCG ATG CTC GAT CAG TGG GCT AGG TGC GTA GCG GTC TG/3' with molecular weight 13,871.8 g/mol and melting point 71.4 °C. Dopamine solutions were prepared by mixing dopamine hydrochloride in PBS with 10 % wt *L*-ascorbic acid and then serially diluted for the desired concentration. Ascorbic acid was added to decelerate the oxidation of dopamine.[32,33]

Nanopipette fabrication and characterization

Nanopipettes were fabricated from quartz capillaries with filament (o.d. 1 mm, i.d. 0.5 mm, 10 cm length, World Precision Instruments QF100-50-10). The capillaries were transformed into nanopipettes using a laser puller (P2000, Sutter Instruments). For reproducible nanopipettes, the laser puller was preheated for at least 1 h prior to use and a pull was activated without fastening a capillary, prior to nanopipette fabrication. To achieve ∼10 nm diameter orifices, the following parameters were used: (line 1) Heat 750, Filament 4, Velocity 40, Delay 150, and Pull 80; (line 2) Heat 700, Filament 3, Velocity 60, Delay 135, Pull 180. We note that these parameters may vary from instrument-to-instrument[34,35] and requires fine tuning and characterization with microscopy to confirm nanopore sizes.

Aptamer functionalization

DNA sequences were functionalized on the inside of the quartz nanopipette using a previously reported protocol.[25] Briefly, vapor phase deposition was conducted under vacuum at 40 °C for 1 h to assemble monolayers of (3-aminopropyl)trimethoxysilane (APTMS) on the nanopipette surfaces. Maintaining ambient humidity below 40 % is crucial for monolayer assembly, and silane clogging has been observed if this parameter was disregarded. Subsequently, nanopipettes were filled for 1 h with 1 mM solutions of 3-maleimidobenzoic acid

N-hydroxysuccinimide ester (MBS) dissolved in a 1:9 (v/v) mixture of dimethyl sulfoxide and PBS. Aptamer disulfide bonds were reduced for 1 h at room temperature using a 50-fold excess of tris(2-carboxyethyl) phosphine (TCEP) relative to DNA aptamer concentration. The DNA solution was diluted to 5 μM in 1x PBS and cleaned to remove unreacted TCEP and cleaved protective groups, using ZebaTM spin desalting columns (7K MWCO, 0.5 mL, ThermoFisher Scientific AG, Reinach, Switzerland). The purified DNA solution was then heated up to 95 °C for 5 min and then renatured by cooling to room temperature to ensure unhybridized sequences in optimal conformations for surface assembly. The MBS solution was removed from the nanopipettes and the sensors were rinsed with 1x PBS. Then, the prepared aptamer solution was incubated for a minimum of 2 h to ensure functionalization to the nanopipette surface. Prior to storage or experimental use, the aptamer solution was removed and the sensors were rinsed three-fold with PBS. Nanopipettes were stored filled with Milli-Q water to reduce etching of the quartz[36] and were stored at 4 °C in high humidity environments to prevent solution evaporation, which may lead to nanoscale tip breakage upon salt crystal formation. Filling and emptying of the nanopipettes was enabled by MicroFil syringe tips (World Precision Instruments, Sarasota, FL).

Sensing measurements *via* aptamer-modified nanopipettes

Current measurement was enabled by two Ag/AgCl quasi-reference counter electrodes fabricated in house. One electrode was positioned inside the nanopipette and another in the bulk solution. The current was measured *via* a custom-built high gain current amplifier and the data recorded using a custom written LabVIEW interface (2017, National Instruments), based on WEC-SPM package provided by Warwick Electrochemistry and Interfaces Group. Data was collected using an FPGA card PCIe-7852R (National Instruments). The current magnitudes and potentials reported in the manuscript are denoted with respect to the electrode in the solution bulk. Cyclic voltammograms were acquired by sweeping voltage at 0.2 V s^{-1} voltage sweep rate.

Quartz crystal microbalance with dissipation monitoring (QCM-D)

The QSense E4 (Biolin Scientific) was used for QCM-D measurements and thiolated aptamers were assembled on QSense gold chips (QSX 301). The chips underwent a rigorous cleaning procedure consisting of 2 min sonication cycles in the following solutions chronologically: isopropanol, acetone, and Milli-Q water. The chips were dried using pressurized nitrogen and then ozone cleaned for 30 min. The QCM-D chip was then sandwiched between two electrodes that apply a voltage to excite the piezoelectric material at its resonance frequency. A winding channel at the flow cell inlet ensures a stable liquid temperature of 24 °C upon contacting the chip surface. The signal from the 3rd harmonic is shown in all graphs. Further details of the measurement protocols and mathematical calculations for extracting the change in monolayer height from the ΔF is available in the Supporting Information SI-1.

Molecular dynamics simulations of aptamer structures

The single-stranded dopamine and serotonin DNA aptamers were first modeled with the MacroMoleculeBuilder command line tool v2.17.[37] The final state of these resulting structures were used as a starting point for the MDS. The MDS of the dopamine and serotonin aptamers and the interactions with their respective targets were performed in Gromacs using the AMBER99SB-ildn force field. The aptamers were placed in the center of a water box of suitable dimensions according to the size of the different aptamers. Then, the respective analyte, dopamine or serotonin, was inserted into the box, with a 1 Å distance between the box surface and the aptamer. Afterwards, ions and water molecules represented using the transferable intermolecular potential with 3 points (TIP3P) model, were inserted into the box.

AmberTools in Gromacs was used to generate the analyte topology files. By applying the steepest descent algorithm and considering periodic boundary conditions (PBC) in all directions, energy minimization was performed. The systems were equilibrated in NVT (where the constant number (N), volume (V), and temperature (T), respectively) and NPT (con-

stant number (N), pressure (P), and temperature (T), respectively) and assembled with a time step of 2 fs for 100 ps. Finally, the simulation was performed at room temperature and pressure: 294 K and 1.01 atm for 200 ns. The MDS were performed using high performance computing (CINECA). Gromacs tools were used to analyze the trajectories of conformational change (*e.g.*, radius of gyration, RMSD) of the MDS. Further details of the RMSD calculations and intermolecular interactions between the aptamer and analyte can be found in the Supporting Information SI-2.

Finite element method simulations

Rectifying behavior of the ionic current through nanopipettes was modeled using finite element method software package Comsol Multiphysics (version 6.0) with Transport of Diluted Species and Electrostatics modules. Further details of the model geometry, equation formulation, mesh, *etc.* are available in the Supporting Information SI-3.

Statistics

All statistics were carried out using GraphPad Prism 9 (GraphPad Software Inc., San Diego). Data are reported as means ± standard errors of the means with probabilities $P<0.05$ considered statistically significant. Comparative data was evaluated by one-way analysis of variance followed by Tukey's multiple group comparisons.

Results and discussion

Specific Dopamine Sensing *via* Aptamer-Modified Nanopipettes

The current flux through the nanopore is measured upon application of a bias between the two Ag/AgCl quasi-reference electrodes: one inside the nanopipette and one in the bulk solution (Figure 1a). Dopamine-specific DNA aptamers were functionalized using sequential

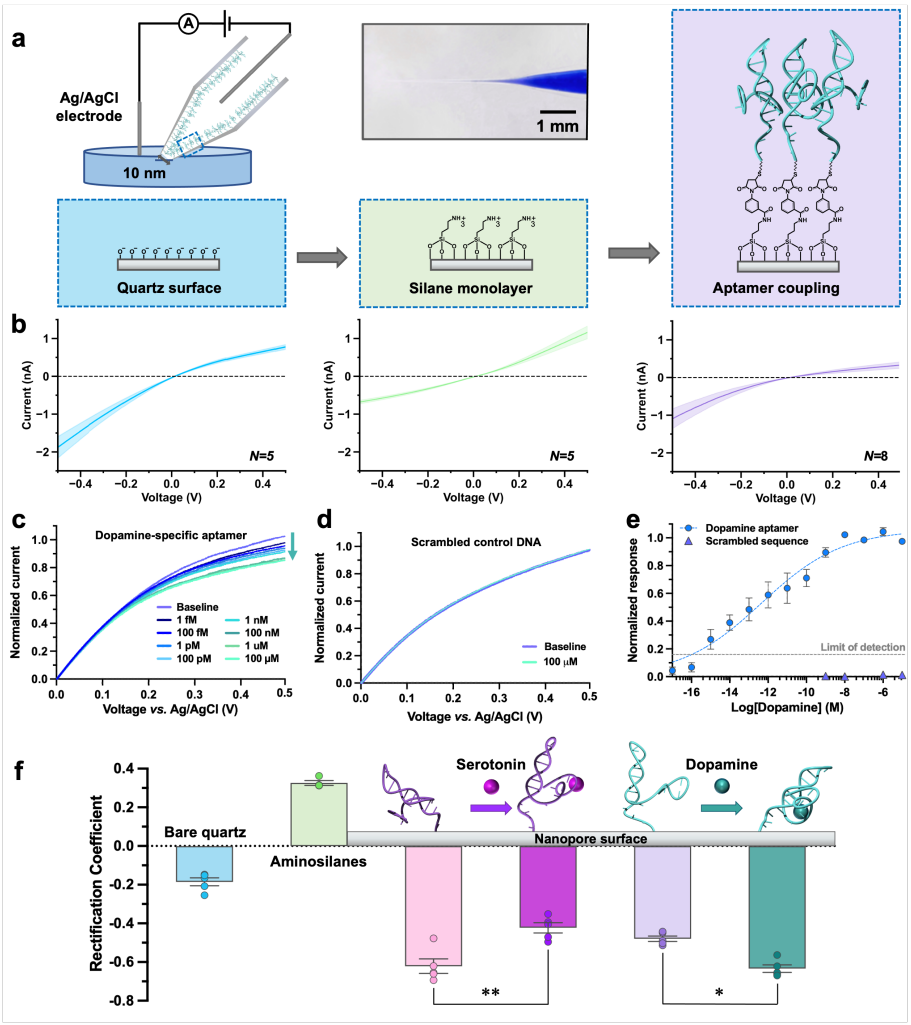

Figure 1: (a) Dopamine aptamer-modified nanopipette sensing schematic and functionalization protocol. (b) Dopamine aptamers are functionalized through sequential surface chemistry that can be tracked using the ion current rectification (ICR) effect manifested as asymmetric current *vs.* voltage curves. Negative charges on bare quartz nanopipettes (N=5) are inverted to positive upon assembly of aminosilanes (N=5). Coupling of negatively charged aptamers leads to higher rectification behavior (N=8).The solid line represents the average and the shaded area the standard error of the mean. (c) Concentration-specific response of dopamine sensors in 1x phosphate buffered silane (PBS) with increasing dopamine amounts observed in cyclic voltammograms (CV). (d) Sensors functionalized with scrambled control DNA resulted in negligible changes compared to baseline, indicative of sequence specificity. (e) Values extracted at +0.5 V from the dopamine-specific CVs (blue circles) were used to plot a calibration curve that shows dopamine detection in the 1 fM - 100 pM range. Scrambled control sensors (purple triangles) showed negligible responses (each point is an average of N=5 CVs and for N=5 independent sensors). The limit of detection was calculated as the signal at zero analyte concentration plus three times its standard deviation. The dotted line is drawn to guide the eye but does not represent classical equilibrium binding. (f) The rectification coefficient *(r)* was calculated from the ICR. For serotonin aptamers, the r value becomes less negative upon serotonin recognition [F(8)=4.301, P<0.01]. In contrast, for dopamine aptamers, the r value becomes more negative upon dopamine capture [F(8)=3.877, P<0.05]. Error bars represent standard errors of the mean for N=5 sensors.

surface chemistry on the inner wall of quartz capillaries with *ca.* 10 nm orifices. The nanopore opening size was previously visualized using transmission electron microscopy.[25] Further, finite element method simulations of the ionic flow through the nanopore corroborated this pore size - the experimental electrical resistance value of 367 MOhm, suggests an opening of 9.2 nm (Supporting Information, SI-3). Ion transport through nanopipettes shows non-Ohmic behavior, where ionic current in one direction is favored due to the influence of an asymmetric electrical double layer in a confined area.[38] This non-linear, diode-like effect observed in the current-voltage curves is called ion current rectification (ICR), which is influenced by the surface charge inside the nanopore when the pore size and geometry are kept constant.[39–41] As shown in Figure 1b, from a bare quartz surface with a slightly negative surface charge due to deprotonated hydroxyl groups, the ICR is slightly negative, implying that the ionic transport is favored at negative applied potentials. Upon assembly of positively charged aminosilanes, the ICR is inverted. Coupling of aptamers returns the ICR to negative rectification with a distinctly curved shape, due to the phosphate backbone of the DNA. Tracking the ICR is a route to ensure optimal starting nanopore sizes post fabrication and effective surface modification in subsequent steps to increase functional sensor yield.

Upon exposure of the dopamine aptamer-modified nanopipette to increasing concentrations of dopamine, the sensor showed a decrease in the current response from baseline (Figure 1c). Alternatively, nanopipettes modified with control sequences designed to have the same number and type of nucleotides as the specific aptamer but in a scrambled order to hinder dopamine recognition, showed minimal response to high dopamine concentrations (100 μM, Figure 1d). Design of a control sensor that has the same chemical signature as the specific dopamine sensor is critical to conduct differential measurements in complex environments.[42] Sequence specificity is further demonstrated in the calibration curve where high amounts of dopamine result in negligible responses for the control sensor while dopamine sensors show a concentration-dependent response (Figure 1e). The dopamine aptamer-modified nanopipettes were sensitive to dopamine amounts in the fM - pM concentration range with

a limit of detection of 1 fM and saturation at 1 nM.

The dopamine aptamer binding affinity (K_d) has been reported as 150 nM.[23] The observed non-linear behavior and detection limit orders of magnitude below the K_d suggests that aptamer-modified nanopipettes are non-equilibrium sensors. Shift from conventional equilibrium behavior may arise from the sensors conical geometry, where the frequency of target rebinding events are higher at the most confined tip region compared to unbinding and release of targets, which may be more prominent further away from the tip that tapers to larger volumes. Single molecules captured from a larger volume and concentrated at the nanopipette tip has been shown to enable fM detection limits.[43] Inducing mass transport of charged molecules like dopamine through the nanopore by applied voltages, drives the analyte trajectory through an aptamer-filled column, thus augmenting molecular interactions. Macromolecular crowding has been shown to enhance the sensitivity through cooperative effects between electrolytes and polymers.[44,45] Increased sensitivity to analyte translocations in nanopipettes was explained by the cationic binding properties of the polymer (poly(ethylene) glycol), which would be analogous for the negatively charged DNA aptamers utilized in this work.

Linking Rectification to Aptamer Structure-Switching Dynamics

Prior investigations with serotonin[25] and ATP[22] aptamer-modified nanopipettes suggested a detection mechanism relying on aptamer structure-switching dynamics. The aptamers gate the ionic flux due to conformational changes upon exposure to the small-molecule target. The serotonin aptamer-modified nanopipettes consistently showed an *increase* in the current response from baseline with increasing concentration of serotonin.[25,26] On the contrary, in this work, the dopamine aptamer-modified nanopipettes showed a *decrease* in the current response from baseline, upon specific recognition of dopamine (Figure 1f). This divergent behavior in sensor response is reminiscent of what was observed on the surface of field-effect transistor biosensors, which was the first platform to which these neurotransmitter aptamers

were integrated.[23] For the n-type field-effect transistors, an *increase* in current for the serotonin aptamer was correlated to the negatively charged DNA backbone moving away from the surface, which increased transconductance. Alternatively, a *decrease* in current for the dopamine aptamer was attributed to the DNA moving closer to the sensor surface, inducing electrostatic repulsion of charge carriers. Thus, we hypothesized that the opposite directionality observed in the nanopipette sensors is driven by the divergent structure-switching of aptamers inside the confined nanopore.

To investigate this hypothesis, we extracted the rectification coefficient (r) from the current-voltage (I-V) curves, a value that enables direct comparisons of surface charge at the walls of the nanopipette.[46] As aptamer conformational changes rearrange negative charge densities at the surfaces to which they are covalently bound, we expected the r value to be influenced in a target-specific manner. This coefficient is calculated by taking the logarithm of the ratio of the absolute values of the current measured at a positively applied voltage, by the current at the corresponding negative voltage:

$$r = log(|I_{V+}/I_{V-}|)$$

The r value changes from -0.2 ± 0.03 for bare quartz surfaces to +0.3 ± 0.02 for aminosilanized nanopipettes as expected based on the surface functional groups (Figure 1e). For the serotonin aptamer-modified sensor, the r value becomes less negative, from -0.7 ± 0.03 to -0.4 ± 0.06 upon exposure to serotonin. Conversely, the r value of the dopamine aptamer-modified sensor becomes increasingly negative upon dopamine capture from -0.5 ± 0.03 to -0.6 ± 0.05. These results indicate that serotonin *vs.* dopamine aptamers alter the surface charge density in opposite directions upon target recognition within the nanopore.

Tracking Aptamer Conformations *via* Quartz Crystal Microbalance

To corroborate our findings concerning the directionality of current change upon target recognition with a complementary methodology, QCM-D was employed. While measuring the binding of molecules with low molecular weights directly using QCM-D is challenging,[4] aptamer conformational dynamics that modify the hydration layer at the surface of the sensor can be harnessed to amplify the signal of small-molecule binding.[47] The serotonin aptamers measured by QCM-D resulted in an ∼1.2 nm elongation upon serotonin capture.[25] A comparative study with the dopamine aptamer gives insight into both the directionality and magnitude of conformational dynamics.

Dopamine aptamer assembly on the QCM-D substrate was confirmed by a decrease in frequency of 23.7 Hz (Figure 2a) and an increase in dissipation of 0.9 x 10^{-6} (Figure S1a) indicative of an assembled rigid monolayer with a height of 4.1 nm, calculated *via* the Sauerbrey equation (Figure 2b).[48,49] Rinsing the surface post-assembly resulted in negligible changes in frequency, confirming the covalent assembly of aptamers on the surface. Upon exposure to dopamine, a frequency increase of ∼3 Hz was observed (Figure 2c), which is in the opposite direction to what was observed for the serotonin aptamers upon target binding.[25] This frequency increase translates to a decrease in aptamer height of ∼0.6 nm (Figure 2d), which is indicative of the aptamers adopting more compact secondary structures upon dopamine binding, leading to loss of water molecules from the aptamer monolayer.[47] The return to original baseline upon rinsing with buffer, demonstrates the reversible unbinding of captured dopamine.

We demonstrated the reproducibility of this binding and unbinding behavior three repeated times on a single QCM-D sensor (Figure S1b) and over N=6 measurements conducted with three different chips (Figure S1c). When repeating this procedure on a chip functionalized with the scrambled control DNA, negligible change in frequency was observed upon exposure to equal amounts of dopamine, indicating target-specific structural rearrangement (Figure S1d). Further, injection of the PBS buffer as well as incubation of structurally similar

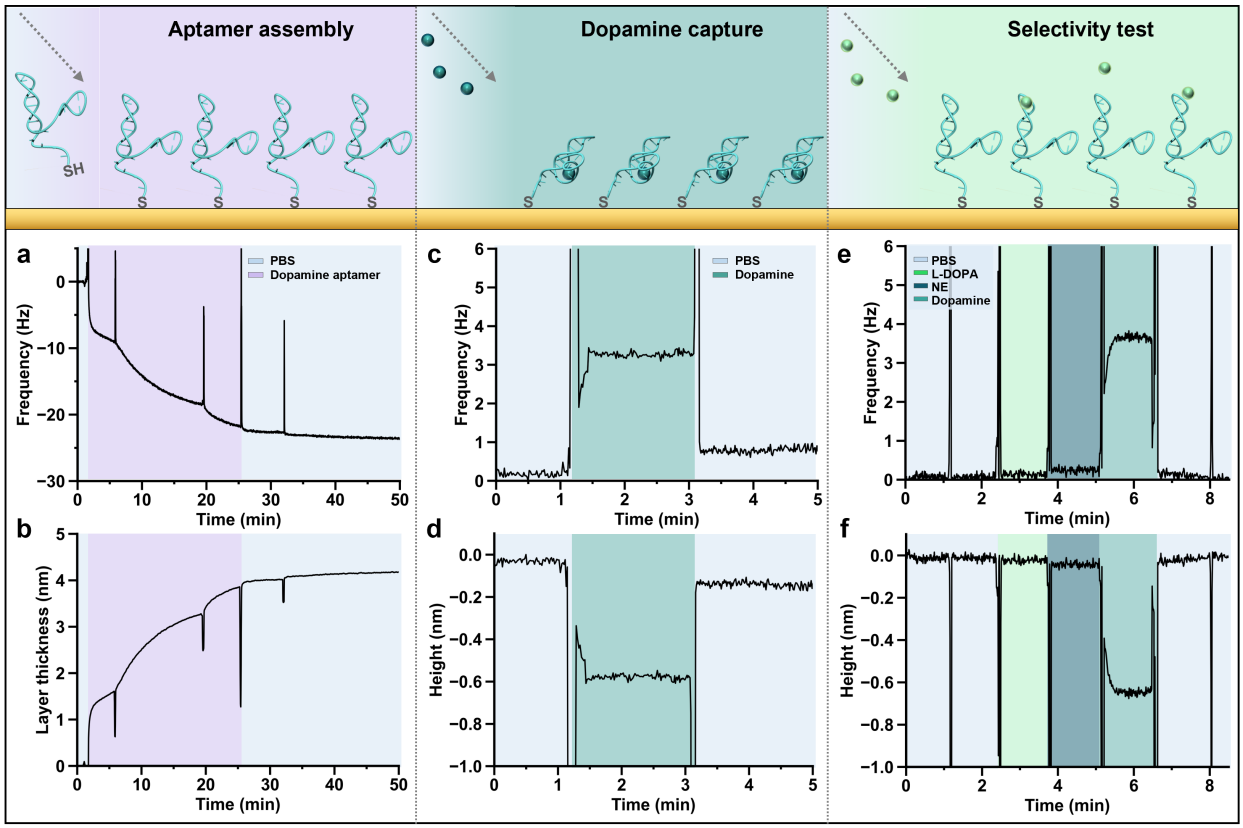

Figure 2: (a) Dopamine aptamer assembly in phosphate buffered saline (PBS) results in a frequency decrease of 23.7 Hz (b) The Sauerbrey equation calculates an assembled aptamer monolayer of 4.1 nm. (c) Exposure of aptamer-modified substrates to 100 μM dopamine led to a reversible increase in frequency of 3.3 Hz. (d) This frequency change translates to a 0.6 nm compression in the aptamer layer upon dopamine recognition based on the Sauerbrey equation. (e) Neither injection of PBS nor 100 μM of nonspecific molecules (*L*-Dopa and Norepinephrine (NE)) showed baseline changes while subsequent addition of dopamine exhibited the characteristic increase in frequency. (f) Despite prior exposure to nonspecific molecules, the dopamine aptamer compresses upon target recognition.

molecules (*L*-DOPA and norepinephrine) resulted in a stable baseline (Figure 2e,f). The subsequent incubation of dopamine, resulted in a frequency increase of comparable magnitude when the aptamer-modified chip was tested solely with dopamine, indicative of negligible interference from prior exposure to nonspecific molecules.

Simulating Target-Specific Aptamer Conformational Changes

Molecular dynamics simulations (MDS) were conducted to corroborate the nanopipette sensing results and QCM-D measurements by modeling the structure-switching dynamics of aptamers upon interactions with the neurotransmitter analytes. In the MDS, the aptamers were constrained at the 5' end (typically modified with thiol groups for surface attachment) to mimic covalently-tethered states with reduced degrees of molecular freedom on the inside of the nanopores. The conformational stability of the aptamers can be determined by the deviations in the root mean square deviation (RMSD) within the simulation time interval - smaller deviations indicate higher structural stability. The conformation dynamics were simulated for an interval of 100 ns, which guaranteed observation of the system in a stable state based on monitoring the RMSD (Figure S2).

The binding of the aptamer with a specific neurotransmitter target was monitored by MDS over the same time interval. Analysis of the aptamer binding phenomena elucidates the interaction of individual nucleobases involved in target recognition and the resulting intermolecular interactions. Analysis revealed that the dopamine aptamer—target complex was maintained *via* four stable hydrogen bonds, electrostatic interactions (Pi-Anion, Pi-Pi-T-shaped, salt-bridge), and hydrophobic interactions (Figure S3a). Specifically, hydrogen bonds formed between the hydrogens of dopamine and the aptamer nucleobases A28, A30, and G33 at distances of 3.12 Å, 4.42 Å, and 3.08 Å, respectively, constitute the binding pocket (Figure 3a). Moreover, the primary amine (protonated at physiological pH) of the dopamine interacted electrostatically with the nucleobases G33 (Pi-cation), A35 (salt-bridge), and with A27 (Pi-anion) (Figure 3b). Further, hydrophobic Pi-Pi T-shaped interactions between G29

and the aromatic moiety of dopamine can be observed.

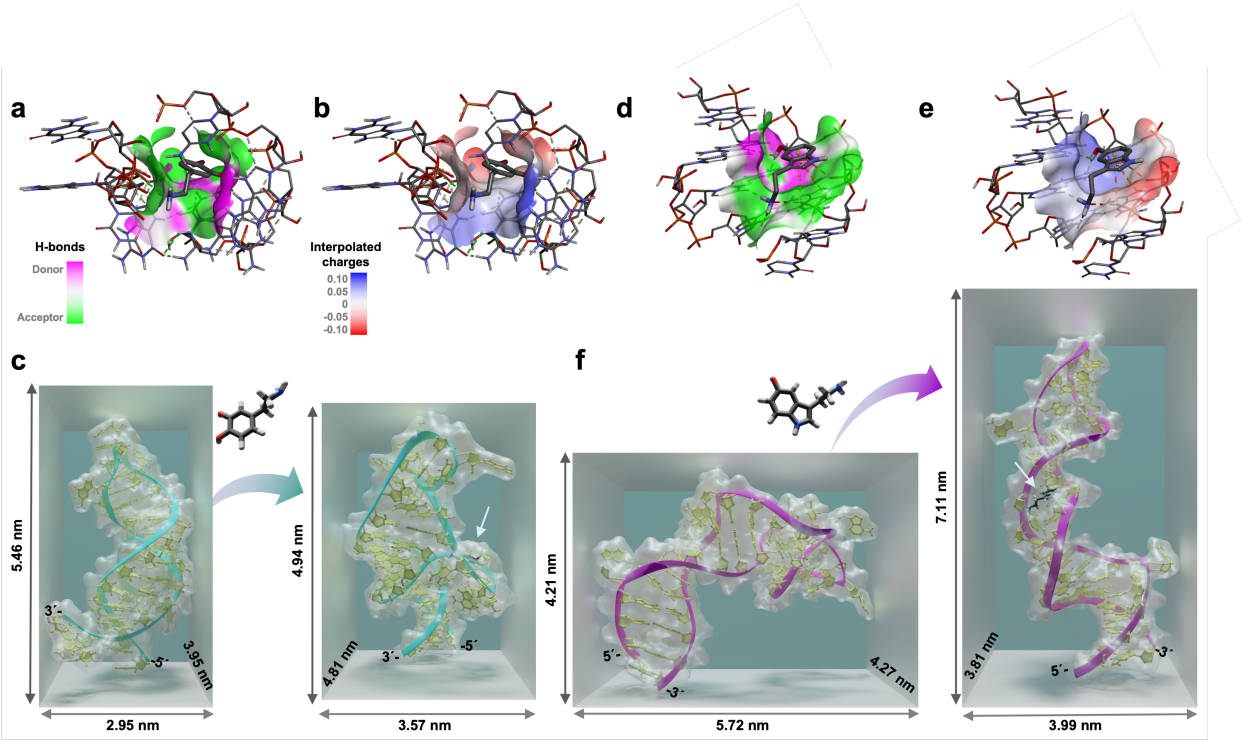

Figure 3: (a) Hydrogen bonding and (b) interpolated charges (blue = more positive, and red = more negative) interactions between the dopamine aptamer and dopamine molecule that constitutes the binding pocket. (c) Extracted 3-D conformations of the dopamine aptamer in the absence (left) and presence (right) of dopamine obtained from 100 ns molecular dynamic simulations (MDS) (d) The hydrogen bonding and (e) interpolated charges between the serotonin aptamer and serotonin molecule. (f) 3-D structure of serotonin aptamer in the absence (left) and presence (right) of serotonin obtained from 100 ns MDS. In both bound-states for the dopamine and serotonin aptamers, an arrow is added as a guide to the eye to visualize the binding location of the respective analyte. All aptamer sequences were confined at the 5' end to mimic surface tethering. To improve the visibility, all water molecules and ions inside the simulation box were removed.

From these intermolecular interactions, where the bases A28, A30, G33, A35, A27, and G29 interact strongly with the dopamine molecule, it can be inferred that the binding takes place inside the asymmetric interior loop of the dopamine aptamer. The 3-D structure of dopamine aptamer in the absence and presence of dopamine was extracted at the end of the MDS (Figure 3c). According to this visualization, the dopamine binding site is located at the distal stem-loop (or hairpin loop). Dopamine binding led to a conformational change where

the aptamer-target complex compresses by 0.6 nm, comparable to the findings in QCM-D (Figure 2d).

Target-specific interactions for the serotonin aptamer was also investigated *via* MDS to interrogate the opposite behaviors observed in the serotonin *vs.* dopamine sensors. The aptamer-serotonin complex consists of four stable hydrogen bonds and electrostatic interactions (Pi-Anion, favorable acceptor-acceptor, and van der Waals) (Figure S3b). Explicitly, the binding pocket was composed of hydrogen bonds formed between the hydrogens of the serotonin and the G19, G20, T26, and G27 aptamer nucleotides with a distance of 2.12 Å, 2.59 Å, 1.89 Å, and 2.79 Å, respectively (Figure 3d). Moreover, electrostatic interactions between the nucleotide A17 and the 6-membered ring of the serotonin, and between the nucleotide G18 and the primary amine of serotonin were observed (Figure 3e and S3b). The 3-D structures of the free serotonin aptamer and the target-bound state with the serotonin molecule in the distal stem loop were extracted (Figure 3f). The MDS indicates that the serotonin aptamer backbone elongates upon serotonin binding, in agreement with previous experimental analyses.[23]

Modeling Aptamer Conformational Changes in Nanopores

Experimental results by QCM-D and theoretical analysis by MDS both indicate that the conformational changes of aptamer molecules modulate the measured ion current changes in nanopipette sensors. To connect our findings on the aptamer structure-switching dynamics to the ionic current modulation through nanopores, a finite element model was designed. The model consisted of a solid nanopore sensor (geometry determined from electron microscopy images) modified with an ion-permeable charged layer with variable thickness, representing the aptamers. We aimed to interrogate the effect of altering the aptamer layer charge density on the rectifying behavior of the nanopore sensors. Based on our modeling with the serotonin aptamer-modified nanopipettes,[26] we expected the signal transduction through the nanopore to be determined by two phenomena: (i) variation of the stored charge density in the layer

of the aptamer molecules at the nanopore walls, and (ii) changes in the aptamer layer permeability for ions carrying the current. The former occurs as the expansion/contraction of the aptamer layer can cause a proportional decrease/increase in the number of charges per unit volume respectively, even when assuming no overall change in the total number of charges.

Both the QCM-D and MDS indicated that the dopamine aptamer layer compresses upon target recognition. The values extracted from the MDS, for the free aptamer (5.5 nm) and dopamine-bound aptamer (4.9 nm) were used to approximate the change in the charge density in the dopamine aptamer layer. An increase in the charge density by ∼11 % (proportional to the layer thickness change), was used as a parameter in the finite element model (Figure S4). The simulation for the dopamine aptamer-modified nanopipettes indicated that the contraction of the charged aptamer layer on nanopore walls, resulted in stronger rectification and a slight decrease of the ion current at positive voltages (Supporting Information SI-3, Figure S6). This trend matches what was observed in the experiments upon sensor exposure to dopamine.

However, similarly to what was observed with the serotonin aptamer-modified sensors,[26] the charge density variation alone did not account for the experimentally observed changes of the current magnitude. For the dopamine sensors, we hypothesize that the contraction of the dopamine aptamer layer leads to a more compact and hence less permeable medium, through which ions are transported with a smaller diffusion constant.[50] When a proportional reduction of the diffusion coefficient of ions is introduced to the charged layer of aptamers in the model, a further reduction of the ion current through the nanopipette is observed (Figure S7). In this case, the total change of the ionic current for the free dopamine aptamer *vs.* dopamine aptamer-target complex approaches the experimentally observed 11 % current decrease for 1 nM analyte. However, the difference in curve shapes observed in the model compared to the experimental I-V characteristics, suggests a qualitative agreement rather than quantitative comparison.

The finite element model appears to be generalizable for different aptamers when the sequence-specific conformational dynamics is well understood. While the behavior and the measured signals follow an opposing trend for the dopamine *vs.* serotonin aptamers, the mechanism behind the signal transduction bears close similarities. Conformational change upon analyte binding appears to cause a contraction (dopamine) or expansion (serotonin) of the charged aptamer layer, accompanied by a change in mass transport (altered diffusion constant) through this medium. Interestingly, these factors are most pronounced for both negatively charged aptamers only in the positive side of the I-V curve. Alternatively, at negative biases, the effect of changing the thickness of the charged layer and the influence of altering the ion diffusivity tends to cancel each other out, resulting in a lack of observable trend for sensing.

In addition to finite element modeling, we calculated the Dukhin number (Du), which identifies the ratio of the surface *vs.* bulk conductivity occurring within the aptamer-modified nanopore.[51] The approximated Du value of 8.4 and 4.0 for the dopamine and serotonin aptamer-functionalized nanopores, respectively (calculations can be found in Supporting Information, SI-4), implies that surface conductivity dominates *vs.* the bulk (represented in Figure 4). The measured current through the nanopore is primarily driven by the ionic flux that resides within the Debye layer at the walls of the nanopore (corresponding to ∼0.7 nm in 1x PBS).[51] Thus, when the dopamine aptamers contract upon target recognition, this conformational change will influence the ionic conductance along the nanopore walls (represented by the blue arrows in Figure 4), while the bulk ionic flux through the nanopore remains unchanged (black arrows in Figure 4). Moreover, the mobility of solution ions within the DNA layer is contingent on the conformational state of the aptamers. Tighter bundles of DNA reduce ionic permeability.[50,52] Thus, a contracted layer of dopamine aptamers will lead to decreased ionic flux and *vice versa* for the serotonin aptamers that expand upon target capture.

An alternative way to interrogate the influence of the aptamer conformational dynamics

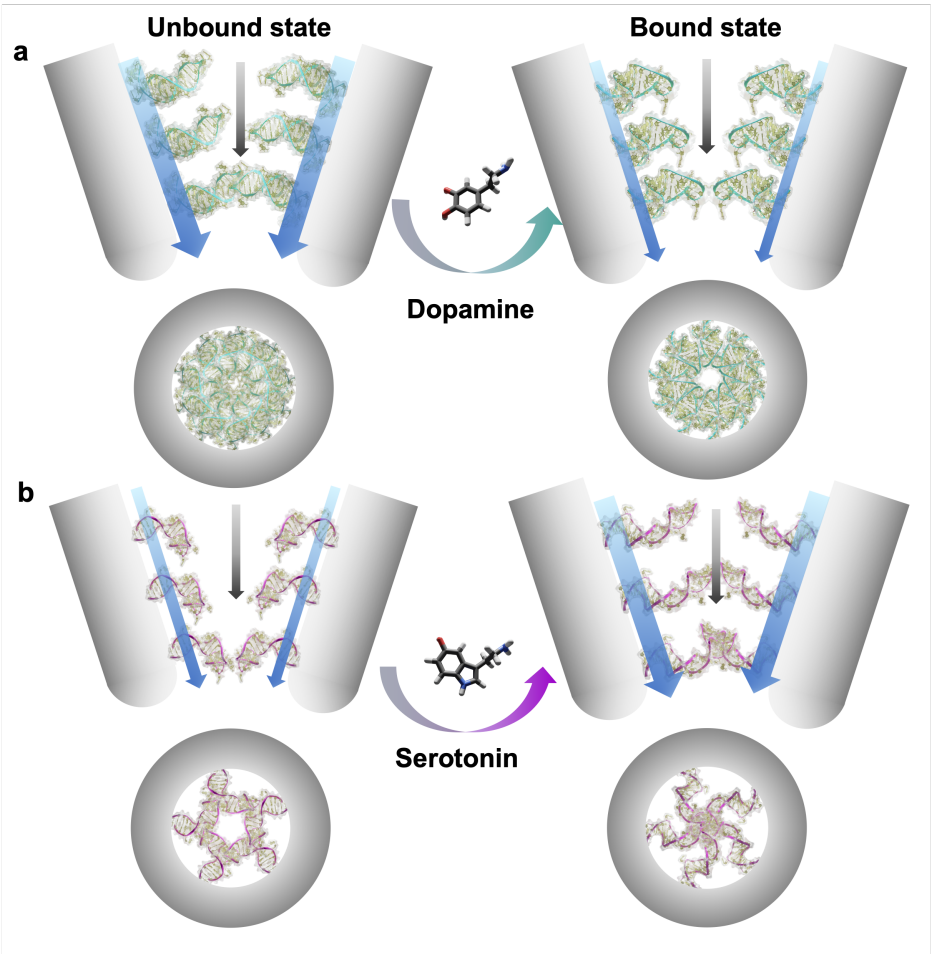

Figure 4: Schematic representation of ionic flux through dopamine and serotonin aptamer-functionalized nanopipettes. (a) Dopamine and (b) serotonin aptamers are shown as immobilized on the walls of the nanopipette from a side-view (top) or when looking inside the 10 nm orifice (bottom). The maximal number of aptamers bound at the tip was estimated by using the minimal required surface corresponding to the bottom rectangle extracted from the molecular dynamic simulation of the free aptamer. The unbound aptamer state is shown on the left and the target-bound state on the right. The respective targets trigger conformational changes altering the charge density and DNA layer thickness inside of the pore. The blue arrows represent the cationic flux along the walls of the nanopipettes, while the black arrows represent the cationic flux of the bulk of the nanopipette. The width of the arrows is used to represent magnitude of the flux under the different DNA conformations.

on the ionic flux through the nanopore, is by calculating the different factors that contribute towards the change in current. The specific conformation of the aptamers influences the charge density of mobile counterions in the nanopore that neutralize the negative DNA backbone. Thus, the experimentally measured current response has contributions from the current excluded by the volume of the 3-D DNA ($I_{excluded}$) and the current that flows through the assembled aptamer layer ($\mathrm{I}_{aptamer}$). These calculations support our prior experimental and theoretical findings (Supporting Information SI-5).[52] By interrogating aptamer structure-switching dynamics extensively through different models and connecting these findings to the observed sensor response, we have improved our understanding of the unique behavior of aptamer-modified nanopore sensors.

Conclusions

In this work, we demonstrated that the target-specific structure switching of aptamers immobilized within nanopores, drive concentration-dependent changes in the sensor response. In addition to the characterization of a novel nanoscale dopamine sensor with femtomolar detection limits, we investigated the fundamental mechanisms governing the modulation of ionic flux through nanopores. In particular, our goal was to understand the opposite directionality of the measured current when comparing aptamer-modified nanopipette sensors targeting two neurotransmitters of comparable mass and equal charge: dopamine and serotonin. Through QCM-D, a complementary surface-based piezoelectric sensor, we confirmed divergent aptamer conformational dynamics upon target binding: dopamine aptamers compress towards the tethered surface, while the inverse (elongation upon target capture) is observed for serotonin aptamers.[25]

To corroborate these experimental findings with theoretical models, we simulated the aptamer structure switching using MDS. Validation of theoretical models that facilitate simulation of aptamer structural dynamics provides a critical layer of control to establish design

rules for aptamer-based nanopore sensors. For example, visualization of the aptamer-target interactions may provide insight into how to optimize aptamer surface densities to minimize steric hindrance or what size nanopores to emply based on magnitude of structure switching.[53,54] We demonstrated how values extracted from the MDS model can be incorporated into finite element models and other mathematical calculations to understand the combined influence of changes in the charge density and ion permeability of the aptamer layer. Such investigations improve our understanding of the complex interactions occurring in confined nanoscale environments.

Aptamer conformational change in nanoscale confinement being the central mechanism that drives small-molecule target detection, endows the sensors with inherent selectivity. Larger nonspecific molecules are occluded from the DNA-filled nanopore and nonspecific small molecules that can enter the pore have minimal effects on the current response as the structure-switching response is target specific. Insight into the fundamental mechanisms of aptamer-modified nanopore biosensors is generalizable for the detection of small molecules. Beyond the development of novel nanotools that bring us closer to unraveling the complexity of brain chemistry, our findings will drive further innovations in biomimetic nanopore technologies. Further, seamless integration of the aptamer-modified nanopipettes as probes into various measurement platforms such as conventional electrophysiology patch clamp setups and scanning probe methodologies is possible, enabling fast sensor translation for diverse applications.[26]

Acknowledgement

The authors thank Prof. Janos Vörös for helpful discussions. A.S. and N. N. thank the ETH Zürich research grant (ETH-13 21-2) and A.D. and D.G. the European Union under the Horizon 2020 Program, FET-Open: DNA-FAIRYLIGHTS, Grant Agreement No. 964995. A.D. also thanks Walter Rocchia for the access to the computation facility. D.M. acknowl-

edges the financial support from the European Research Council (ERC) under the European Union's Horizon 2020 research and innovation programme (Grant Agreement 948238).

Supporting Information Available

References

(1) Ni, S.; Zhuo, Z.; Pan, Y.; Yu, Y.; Li, F.; Liu, J.; Wang, L.; Wu, X.; Li, D.; Wan, Y., et al. Recent progress in aptamer discoveries and modifications for therapeutic applications. *ACS Applied Materials & Interfaces* **2020**, *13*, 9500–9519.

(2) Yu, H.; Alkhamis, O.; Canoura, J.; Liu, Y.; Xiao, Y. Advances and Challenges in Small-Molecule DNA Aptamer Isolation, Characterization, and Sensor Development. *Angewandte Chemie* **2021**, *133*, 16938–16961.

(3) Wang, Z.-J.; Chen, E.-N.; Yang, G.; Zhao, X.-Y.; Qu, F. Research Advances of Aptamers Selection for Small Molecule Targets. *Chinese Journal of Analytical Chemistry* **2020**, *48*, 573–582.

(4) Ruscito, A.; DeRosa, M. C. Small-Molecule Binding Aptamers: Selection Strategies, Characterization, and Applications. *Front. Chem.* **2016**, *4*, 1–14.

(5) McKeague, M.; DeRosa, M. C. Challenges and Opportunities for Small Molecule Aptamer Development. *Journal of Nucleic Acids* **2012**, *2012*, 1–20.

(6) Nakatsuka, N.; Cao, H. H.; Deshayes, S.; Melkonian, A. L.; Kasko, A. M.; Weiss, P. S.; Andrews, A. M. Aptamer Recognition of Multiplexed Small-Molecule-Functionalized Substrates. *ACS Applied Materials & Interfaces* **2018**, *10*, 23490–23500.

(7) Iqbal, S. M.; Akin, D.; Bashir, R. Solid-state nanopore channels with DNA selectivity. *Nature nanotechnology* **2007**, *2*, 243–248.

(8) Ding, S.; Gao, C.; Gu, L.-Q. Capturing single molecules of immunoglobulin and ricin with an aptamer-encoded glass nanopore. *Analytical chemistry* **2009**, *81*, 6649–6655.

(9) Cai, S.; Sze, J. Y.; Ivanov, A. P.; Edel, J. B. Small molecule electro-optical binding assay using nanopores. *Nature communications* **2019**, *10*, 1–9.

(10) Waugh, M.; Briggs, K.; Gunn, D.; Gibeault, M.; King, S.; Ingram, Q.; Jimenez, A. M.; Berryman, S.; Lomovtsev, D.; Andrzejewski, L., et al. Solid-state nanopore fabrication by automated controlled breakdown. *Nature Protocols* **2020**, *15*, 122–143.

(11) Fried, J. P.; Swett, J. L.; Nadappuram, B. P.; Mol, J. A.; Edel, J. B.; Ivanov, A. P.; Yates, J. R. In situ solid-state nanopore fabrication. *Chemical Society Reviews* **2021**, *50*, 4974–4992.

(12) Xue, L.; Yamazaki, H.; Ren, R.; Wanunu, M.; Ivanov, A. P.; Edel, J. B. Solid-state nanopore sensors. *Nature Reviews Materials* **2020**, *5*, 931–951.

(13) Storm, A.; Chen, J.; Ling, X.; Zandbergen, H.; Dekker, C. Fabrication of solid-state nanopores with single-nanometre precision. *Nature materials* **2003**, *2*, 537–540.

(14) Shao, Y.; Mirkin, M. V.; Fish, G.; Kokotov, S.; Palanker, D.; Lewis, A. Nanometer-sized electrochemical sensors. *Analytical Chemistry* **1997**, *69*, 1627–1634.

(15) Hengsteler, J.; Mandal, B.; van Nisselroy, C.; Lau, G. P.; Schlotter, T.; Zambelli, T.; Momotenko, D. Bringing electrochemical three-dimensional printing to the nanoscale. *Nano letters* **2021**, *21*, 9093–9101.

(16) Cai, S.-L.; Cao, S.-H.; Zheng, Y.-B.; Zhao, S.; Yang, J.-L.; Li, Y.-Q. high-affi modulated aptasensor in a single glass conical nanopore. *Biosensors and Bioelectronics* **2015**, *71*, 37–43.

(17) Actis, P.; Rogers, A.; Nivala, J.; Vilozny, B.; Seger, R. A.; Jejelowo, O.; Pourmand, N. Reversible thrombin detection by aptamer functionalized STING sensors. *Biosensors and Bioelectronics* **2011**, *26*, 4503–4507.

(18) Yang, K.-A.; Chun, H.; Zhang, Y.; Pecic, S.; Nakatsuka, N.; Andrews, A. M.; Worgall, T. S.; Stojanovic, M. N. High-affinity nucleic-acid-based receptors for steroids. *ACS chemical biology* **2017**, *12*, 3103–3112.

(19) Sanford, A. A.; Rangel, A. E.; Feagin, T. A.; Lowery, R. G.; Argueta-Gonzalez, H. S.; Heemstra, J. M. RE-SELEX: restriction enzyme-based evolution of structure-switching aptamer biosensors. *Chemical science* **2021**, *12*, 11692–11702.

(20) Feagin, T. A.; Maganzini, N.; Soh, H. T. Strategies for creating structure-switching aptamers. *ACS sensors* **2018**, *3*, 1611–1615.

(21) Abelow, A. E.; Schepelina, O.; White, R. J.; Vallée-Bélisle, A.; Plaxco, K. W.; Zharov, I. Biomimetic glass nanopores employing aptamer gates responsive to a small molecule. *Chemical communications* **2010**, *46*, 7984–7986.

(22) Cai, S.-L.; Zheng, Y.-B.; Cao, S.-H.; Cai, X.-H.; Li, Y.-Q. A conformation and charge co-modulated ultrasensitive biomimetic ion channel. *Chemical Communications* **2016**, *52*, 12450–12453.

(23) Nakatsuka, N.; Yang, K.-A.; Abendroth, J. M.; Cheung, K. M.; Xu, X.; Yang, H.; Zhao, C.; Zhu, B.; Rim, Y. S.; Yang, Y.; Weiss, P. S.; Stojanović, M. N.; Andrews, A. M. Aptamer–field-effect transistors overcome Debye length limitations for small-molecule sensing. *Science* **2018**, *362*, 319–324.

(24) Mayne, L.; Lin, C.-Y.; Christie, S. D.; Siwy, Z. S.; Platt, M. The design and characterization of multifunctional aptamer nanopore sensors. *ACS nano* **2018**, *12*, 4844–4852.

(25) Nakatsuka, N.; Faillétaz, A.; Eggemann, D.; Forró, C.; Vörös, J.; Momotenko, D. Aptamer Conformational Change Enables Serotonin Biosensing with Nanopipettes. *Analytical Chemistry* **2021**, *93*, 4033–4041.

(26) Nakatsuka, N.; Heard, K. J.; Faillétaz, A.; Momotenko, D.; Vörös, J.; Gage, F. H.; Vadodaria, K. C. Sensing serotonin secreted from human serotonergic neurons using aptamer-modified nanopipettes. *Mol Psychiatry* **2021**, *26*, 2753–2763.

(27) Douaki, A.; Garoli, D.; Inam, A. S.; Costa Angeli, M. A.; Cantarella, G.; Rocchia, W.; Wang, J.; Petti, L. P., Luisa Smart Approach for the Design of Highly Selective Aptamer-Based Biosensors. *Biosensors* **2022**, *12*, 574.

(28) Xie, Y.-c.; Eriksson, L. A.; Zhang, R.-b. Molecular dynamics study of the recognition of ATP by nucleic acid aptamers. *Nucleic Acids Research* **2020**, *48*, 6471–6480.

(29) Xiao, J.; Salsbury, F. R. Molecular dynamics simulations of aptamer-binding reveal generalized allostery in thrombin. *Journal of Biomolecular Structure and Dynamics* **2017**, *35*, 3354–3369.

(30) Yan, S.; Peck, J. M.; Ilgu, M.; Nilsen-Hamilton, M.; Lamm, M. H. Sampling Performance of Multiple Independent Molecular Dynamics Simulations of an RNA Aptamer. *ACS Omega* **2020**, *5*, 20187–20201.

(31) Torabi, R.; Bagherzadeh, K.; Ghourchian, H.; Amanlou, M. An investigation on the interaction modes of a single-strand DNA aptamer and RBP4 protein: a molecular dynamic simulations approach. *Org. Biomol. Chem.* **2016**, *14*, 8141–8153.

(32) Du, X.; Li, L.; Behboodi-Sadabad, F.; Welle, A.; Li, J.; Heissler, S.; Zhang, H.; Plumeré, N.; Levkin, P. A. Bio-inspired strategy for controlled dopamine polymerization in basic solutions. *Polym. Chem.* **2017**, *8*, 2145–2151.

(33) Bagga, V.; Dunnett, S. B.; Fricker-Gates, R. A. Ascorbic Acid Increases the Number of Dopamine Neurons In Vitro and in Transplants to the 6-OHDA-Lesioned Rat Brain. *Cell Transplant* **2008**, *17*, 763–773.

(34) Chau, C.; Marcuccio, F.; Soulias, D.; Edwards, M. A.; Tuplin, A.; Radford, S. E.; Hewitt, E.; Actis, P. Probing RNA Conformations Using a Polymer–Electrolyte Solid-State Nanopore. *ACS Nano* **2022**, acsnano.2c08312.

(35) Ren, R.; Sun, M.; Goel, P.; Cai, S.; Kotov, N. A.; Kuang, H.; Xu, C.; Ivanov, A. P.; Edel, J. B. Single-Molecule Binding Assay Using Nanopores and Dimeric NP Conjugates. *Adv. Mater.* **2021**, *33*, 2103067.

(36) Alawami, M. F.; Bošković, F.; Zhu, J.; Chen, K.; Sandler, S. E.; Keyser, U. F. Lifetime of glass nanopores in a PDMS chip for single-molecule sensing. *iScience* **2022**, *25*, 104191.

(37) Flores, S. C.; Sherman, M.; Bruns, C. M.; Eastman, P.; Altman, R. B. Fast flexible modeling of RNA structure using internal coordinates. *IEEE/ACM Transactions on Computational Biology and Bioinformatics* **2010**, *8*, 1247–1257.

(38) Wei, C.; Bard, A. J.; Feldberg, S. W. Current rectification at quartz nanopipet electrodes. *Analytical Chemistry* **1997**, *69*, 4627–4633.

(39) Kubeil, C.; Bund, A. The role of nanopore geometry for the rectification of ionic currents. *The Journal of Physical Chemistry C* **2011**, *115*, 7866–7873.

(40) Siwy, Z. Ion-Current Rectification in Nanopores and Nanotubes with Broken Symmetry. *Advanced Functional Materials* **2006**, *16*, 735–746.

(41) Powell, M. R.; Cleary, L.; Davenport, M.; Shea, K. J.; Siwy, Z. S. Electric-field-induced wetting and dewetting in single hydrophobic nanopores. *Nature nanotechnology* **2011**, *6*, 798–802.

(42) Frutiger, A.; Tanno, A.; Hwu, S.; Tiefenauer, R. F.; Vörös, J.; Nakatsuka, N. Nonspecific Binding—Fundamental Concepts and Consequences for Biosensing Applications. *Chem. Rev.* **2021**, *121*, 8095–8160.

(43) Freedman, K. J.; Otto, L. M.; Ivanov, A. P.; Barik, A.; Oh, S.-H.; Edel, J. B. Nanopore sensing at ultra-low concentrations using single-molecule dielectrophoretic trapping. *Nature communications* **2016**, *7*, 1–9.

(44) Chau, C. C.; Radford, S. E.; Hewitt, E. W.; Actis, P. Macromolecular crowding enhances the detection of DNA and proteins by a solid-state nanopore. *Nano letters* **2020**, *20*, 5553–5561.

(45) Chau, C.; Marcuccio, F.; Soulias, D.; Edwards, M. A.; Tuplin, A.; Radford, S. E.; Hewitt, E.; Actis, P. Probing RNA Conformations Using a Polymer–Electrolyte Solid-State Nanopore. *ACS nano* **2022**,

(46) Wang, Y.; Wang, D.; Mirkin, M. V. Resistive-pulse and rectification sensing with glass and carbon nanopipettes. *Proceedings of the Royal Society A: Mathematical, Physical and Engineering Sciences* **2017**, *473*, 20160931.

(47) Osypova, A.; Thakar, D.; Dejeu, J.; Bonnet, H.; Van der Heyden, A.; Dubacheva, G. V.; Richter, R. P.; Defrancq, E.; Spinelli, N.; Coche-Guérente, L.; Labbé, P. Sensor Based on Aptamer Folding to Detect Low-Molecular Weight Analytes. *Analytical Chemistry* **2015**, *87*, 7566–7574.

(48) Sauerbrey, G. Verwendung von Schwingquarzen zur Wägung dünner Schichten und zur Mikrowägung. *Z. Physik* **1959**, *155*, 206–222.

(49) Vogt, B. D.; Soles, C. L.; Lee, H.-J.; Lin, E. K.; Wu, W.-l. Moisture Absorption and Absorption Kinetics in Polyelectrolyte Films: Influence of Film Thickness. *Langmuir* **2004**, *20*, 1453–1458.

(50) Kesselheim, S.; Müller, W.; Holm, C. Origin of Current Blockades in Nanopore Translocation Experiments. *Phys. Rev. Lett.* **2014**, *112*, 018101.

(51) Poggioli, A. R.; Siria, A.; Bocquet, L. Beyond the Tradeoff: Dynamic Selectivity in Ionic Transport and Current Rectification. *J. Phys. Chem. B* **2019**, *123*, 1171–1185.

(52) Wang, V.; Ermann, N.; Keyser, U. F. Current enhancement in solid-state nanopores depends on three-dimensional DNA structure. *Nano Letters* **2019**, *19*, 5661–5666.

(53) Cao, H. H.; Nakatsuka, N.; Liao, W.-S.; Serino, A. C.; Cheunkar, S.; Yang, H.; Weiss, P. S.; Andrews, A. M. Advancing biocapture substrates via chemical lift-off lithography. *Chemistry of Materials* **2017**, *29*, 6829–6839.

(54) Nakatsuka, N.; Cao, H. H.; Deshayes, S.; Melkonian, A. L.; Kasko, A. M.; Weiss, P. S.; Andrews, A. M. Aptamer recognition of multiplexed small-molecule-functionalized substrates. *ACS applied materials & interfaces* **2018**, *10*, 23490–23500.

TOC Graphic

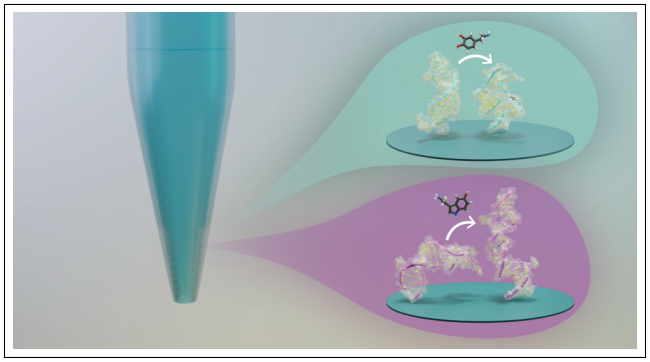

Aptamer Conformational Dynamics Modulate Neurotransmitter Sensing in Nanopores

Annina Stuber,[†] Ali Douaki,[‡] Julian Hengsteler,[†] Denis Buckingham,[†] Dmitry Momotenko,[¶] Denis Garoli,[*,‡] and Nako Nakatsuka[*,†]

†*Laboratory of Biosensors and Bioelectronics, Institute for Biomedical Engineering, ETH Zürich, CH-8092, Switzerland*

‡*Instituto Italiano di Tecnologia, Via Morego 30, 16163, Genova, Italy*

¶*Department of Chemistry, Carl von Ossietzky University of Oldenburg, Oldenburg D-26129,Germany*

E-mail: denis.garoli@iit.it; nakatsuka@biomed.ee.ethz.ch

Contents

SI-1. Quartz crystal microbalance with dissipation monitoring S3

Measurement protocol S3

Calculating monolayer height *via* the Sauerbrey equation S5

SI-2. Molecular dynamic simulations (MDS) S6

Root-mean square deviation (RMSD) S6

Intermolecular interactions in the aptamer binding pocket S7

SI-3. Modeling rectifying behavior of aptamer-modified nanopipettes S8

Model description S8

Estimation of the nanopore opening S11

Effect of charged aptamer layer on measured current through nanopipettes S12

Aptamer layer compression that incorporates change of charge density S13

Aptamer layer compression that incorporates ion permeability S14

SI-4. Dukhin number calculation S15

SI-5. Estimation of theoretical current S16

SI-1. Quartz crystal microbalance with dissipation monitoring

Measurement protocol

A stable baseline was obtained in PBS prior to aptamer assembly. The thiolated DNA sequences were pre-treated following the same procedure as the nanopipette functionalization (cleaving, dilution, purification, heat treatment). The aptamer solution was injected and incubated until the frequency (Figure 3a) and dissipation (Figure S1a) plateaued. Then, covalent binding of the aptamer was challenged by flushing buffer to rinse any unbound sequences. Dopamine prepared with 10 wt % ascorbic acid was exposed to the chip and was then washed away by flushing the buffer. The same surface was used for multiple repeats of dopamine binding and unbinding (Figure S1b). Repeated measures were conducted on N=3 different QCM-D chips for a total of N=6 measurements including retesting on certain chips (Figure S1c). For certain repeated measures, the aptamer solution was incubated overnight on the QCM-D chips rather than assembled *in situ*; both functionalization routes yielded comparable magnitude responses to dopamine. The same procedure was followed using scrambled DNA-modified chips to ensure sequence-specific changes in frequency and dissipation (Figure S1d).

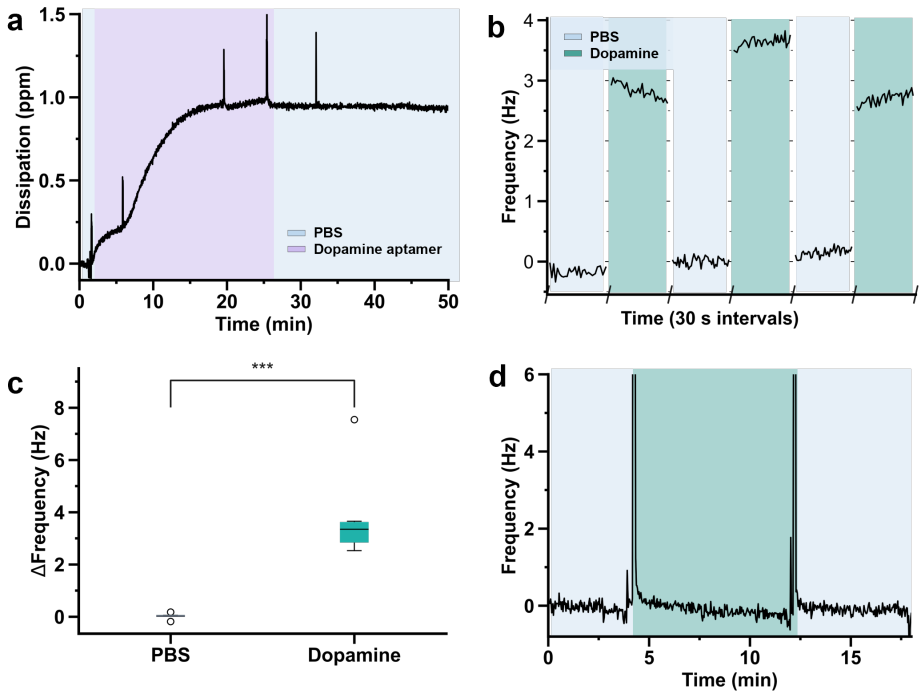

Figure. S1: (a) Dopamine aptamer assembly in phosphate buffered saline (PBS) results in a dissipation increase of ∼1 parts per million (ppm). (b) Three consecutive repeats of switching the solution on a single chip from PBS to dopamine solution demonstrating the reproducibility of the reversible signal due to binding and unbinding of dopamine from the aptamer. (c) The frequency change upon PBS injection *vs.* dopamine injection results in a statistically significant difference (P<0.001) measured on three different QCM-D sensors for a total of N=6 repeated measures. (d) Control measurements run in parallel where 100 μM of dopamine solution is exposed to a QCM-D sensor functionalized with the scrambled DNA sequence (same nucleotides as the specific dopamine aptamer, but in a random order to hinder dopamine recognition), resulted in negiligible changes in the frequency. For all measurements, the 3rd overtone is shown.

Calculating monolayer height *via* the Sauerbrey equation

The change in mass on the quartz crystal can be calculated from a measured change in frequency ($\Delta(f)$) at a specific harmonic (n) as described by the Sauerbrey equation:

$$m_{QCM} = -c\Delta f/n \tag{1}$$

where the mass sensitivity constant, $c = 17.7$ ng/cm^{2}Hz relates to the properties for the 5 MHz quartz crystal chip. The height or the effective distance from the chip surface (d_{eff}) can then be extracted using the equation:

$$d_{eff} = \Delta m/\rho_{\mathrm{H_2O}} \tag{2}$$

where Δm is the change in mass on the chip calculated prior, and $\rho_{\mathrm{H_2O}}$ the density of water molecules displaced upon aptamer assembly or structure switching. This direct relation, linking change of frequency to change in height, is only applicable for quasi-rigid films, which have the required condition that $\Delta D/\Delta f < 4{*}10^{-7}$ Hz^{-1}.[1,2] Our layer is classified as quasi-rigid as the $\Delta D/\Delta f$ of our aptamers assembled on the chip was calculated to be $\sim 1 * 10^{-7}$ Hz^{-1}.

SI-2. Molecular dynamic simulations (MDS)

Root-mean square deviation (RMSD)

The following figure illustrates the change in the RMSD values of dopamine and serotonin aptamers after 100 ns of MDS (Figure S2). The RMSD values of the dopamine and serotonin aptamers were 0.7 nm and 1.2 nm, respectively. These low values show that 100 ns of simulation was enough to reach a stable state, hence, the final MDS shown in the main text (Figure 3) were performed for 100 ns.

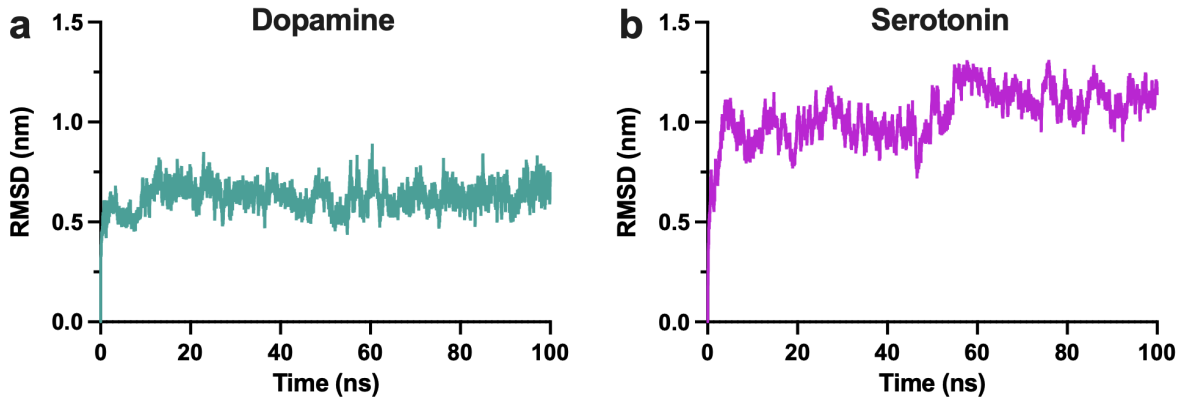

Figure. S2: Root-mean square deviation values of (a) dopamine and (b) serotonin aptamers.

Intermolecular interactions in the aptamer binding pocket

At the end of the 100 ns MDS, the intermolecular interactions between the dopamine aptamer (Figure S3a) and the serotonin aptamer (Figure S3b) and their respective targets were extracted in 2-D.

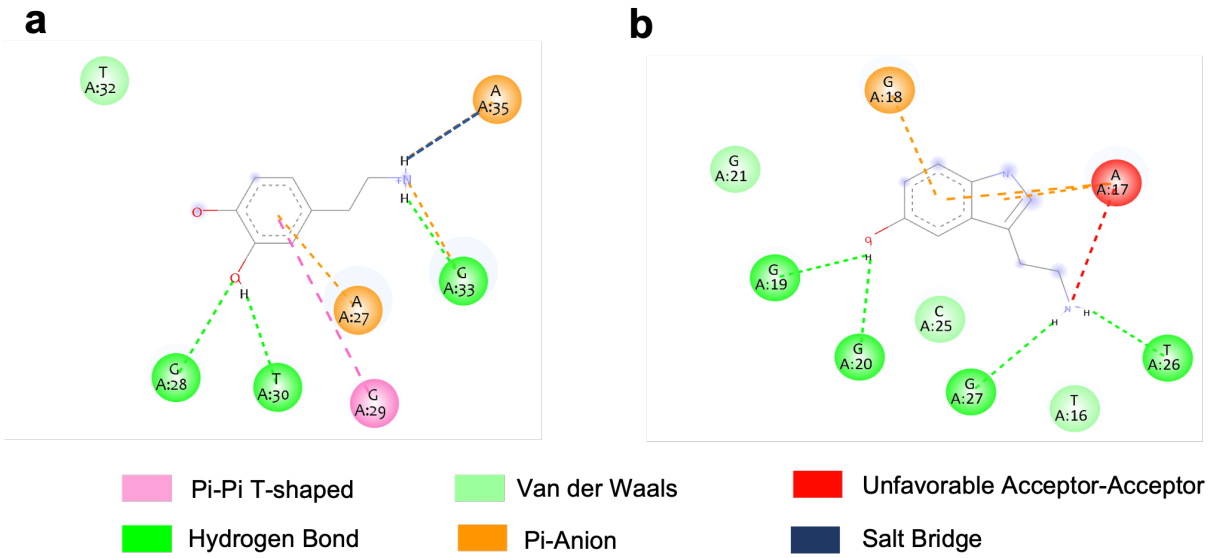

Figure. S3: Interactions established in two dimensions extracted at the end of the 100 ns molecular dynamic simulation for (a) the dopamine aptamer-dopamine interactions and (b) the serotonin aptamer-serotonin interactions. Aptamer nucleotides are represented by spheres of different colours around the structure. Green dashed lines represents the H-bonds, pink the Pi-Pi T-shaped interactions, orange the Pi-anion interactions, red the unfavorable acceptor-acceptor interactions, and blue the salt bridge. The light green nucleotides void of dotted line links, are involved in Van der Waals interactions with the analyte.

SI-3. Modeling rectifying behavior of aptamer-modified nanopipettes

Model description

The finite element model, including the geometry, mesh, and equation formulations is based on our previous work for serotonin-specific aptamer-modified nanopore sensors.[3] The model allows the simulation of ion transport in the presence of an electrical double layer near the pipette walls. Briefly, the simulations domain is built by taking advantage of the geometry's axial symmetry, allowing reduction of computational efforts. The geometry of the computational domain (10 µm x 2 µm) includes a 7.5 µm long section of the nanopipette with appropriate inner and outer half-cone angles, wall thickness at the tip, and an opening radius of 4.6 nm, in accordance with the data from TEM images.[3] The model is discretized into *ca.* 680,000 triangular mesh elements with minimum element size of 0.1 nm. The size of the domain and the nanopipette are optimized to have minimal influence on the numerical result.

The numerical model is formulated using Nernst-Planck:

$$J_i = -D_i \nabla c_i - (z_i F)/RT D_i(T) c_i \nabla \varphi \tag{3}$$

and Poisson equations:

$$\nabla^2 \varphi = -F/(\epsilon\epsilon_0)\Sigma(z_i c_i) \tag{4}$$

that describe ion transport (in the absence of liquid flow) as well as the existence of accumulation of charged species in solution, respectively (Poisson equation allows the electroneutrality to be broken). Here, J_i, D_i, z_i, and c_i, denote the flux, diffusion coefficient, charge number, and local concentration of ionic species i, while φ, F, R, T, ϵ and ϵ_0 specify the electrical potential, Faraday and gas constants, temperature, dielectric constant, and vacuum permittivity, respectively. The model is resolved in the geometry of a nanopipette using appropriate boundary conditions as shown in Figure S4 with boundary conditions specified in Table 1. The thickness of the aptamer layer was varied from 5.5 nm (simulating a

case with no analyte present) to 4.9 nm (in presence of dopamine), based on values extracted from the molecular dynamic simulations (MDS).

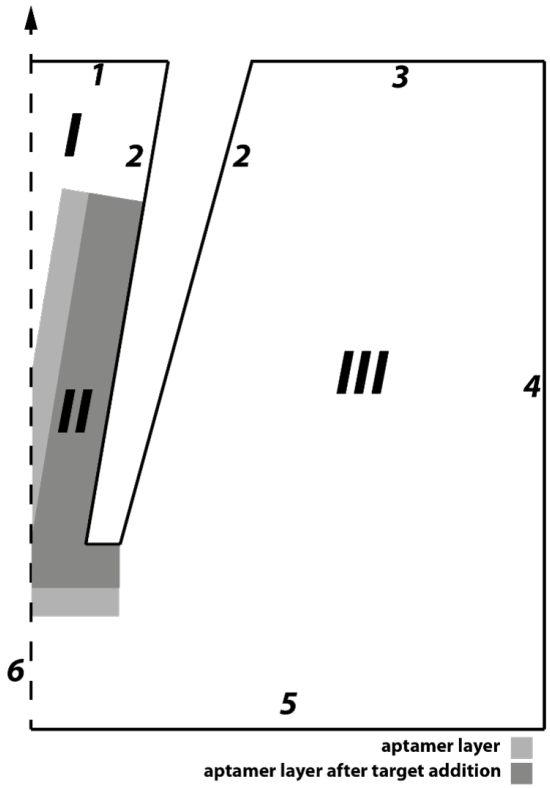

Figure. S4: Schematic representation of the model geometry. Boundary and domain conditions are specified in Table 1 in accordance with the designation on the graph. The change of the aptamer layer (domain II) thickness is illustrated with a grey color shade.

The boundary conditions define electrodes with applied potential and determine bulk solution properties. In particular, the diffusion coefficient inside the aptamer layer (domain II, grey shading in Figure S4) determines the mobility of ions through the layer and is modeled simply as the product of the bulk diffusion constant multiplied by a factor $f \leq 1$. The charge density of the aptamer layer also differs from the bulk electrolyte as the aptamer backbone is highly negatively charged. Individual aptamer charges are taken into account by varying the concentration of these fixed charges in the domain II, while charge density in the bulk solution (domains I and III) is determined only by mobile ions Na^+ and Cl^-.

Table 1: Boundary conditions of the model and specific parameters in model domains. Symbol n denotes the vector normal to the boundary.

Boundary	**Nernst-Planck equation**	**Poisson equation**
1	concentration, c_i = 158 mM	applied potential, φ= bias
2	no flux, -$n \cdot J_j$=0	no charge, $n \cdot \nabla \phi = 0$
3	no flux, -$n \cdot J_j$=0	surface charge, $n \cdot \nabla \phi = \sigma$
4	concentration, c_i=158 mM	ground, φ= 0
5	no flux, -n$\cdot J_j$=0	no charge, $n \cdot \nabla \phi = 0$
6	axial symmetry	axial symmetry
Domain	**Nernst-Planck equation**	**Poisson equation**
I	diffusion coefficient, D_i	charge density, ρ=c_{Na^+}- c_{Cl^-}
II	diffusion coefficient, $f D_i$	charge density, ρ=c_{Na^+}- c_{Cl^-}- c_{fixed}
III	diffusion coefficient, D_i	charge density, ρ=c_{Na^+}- c_{Cl^-}

Estimation of the nanopore opening

To obtain the correct value of the nanopipette opening, the experimental electrical resistance of the bare nanopipette was matched with the simulation results at different opening radii. As the experimental $I - V$ curves reveal significant rectifying behaviour, only a linear part of the experimental voltammogram (between -10 and +10 mV) was used for this purpose. A linear fit of the $I - V$ curve indicated a resistance value of 367 MOhm, which matches numerical result for a pipette with opening diameter 9.2 nm.

Effect of charged aptamer layer on measured current through nanopipettes

The effect of the fixed charges inside the aptamer layer was then modeled for the nanopipette sensors modified with dopamine aptamers prior to exposure to the target (domain II with aptamer layer thickness of 5.5 nm, light gray shading in Figure S4) and post dopamine binding (domain II with aptamer layer thickness of 4.9 nm, dark gray shading in Figure S4). As can be seen from Figure S5, the presence of the fixed charges in the aptamer layer leads to an increase in the ion current rectification when the layer gets progressively more negatively charged (from 0 to 200 mM of charges). Under these assumptions, the thickness of the aptamer layer plays little role in the magnitude of the ionic current - solid (5.5 nm) and dotted (4.9 nm) lines almost coincide.

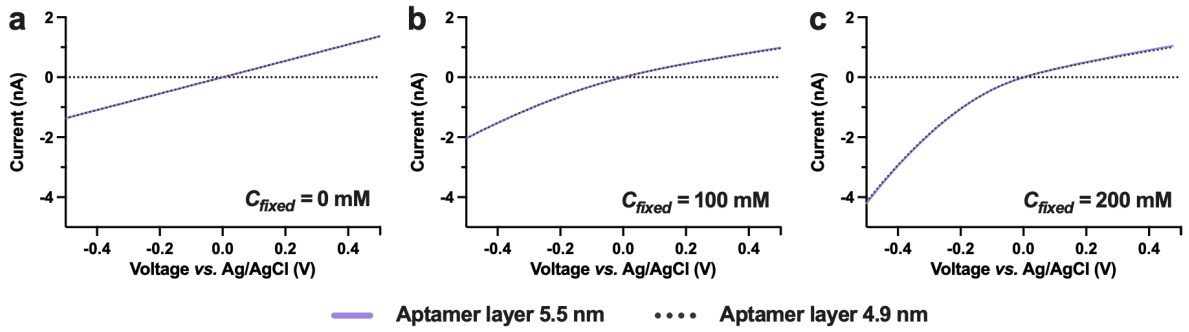

Figure. S5: Simulated $I-V$ characteristics of the nanopipettes with aptamer layer thicknesses of 5.5 (solid purple line) and 4.9 nm (dotted grey line) and concentration of fixed charges within the layer of (a) 0 mM, (b) 100 mM and (c) 200 mM.

Aptamer layer compression that incorporates change of charge density

To understand the effect of aptamer layer compression on the ionic current beyond changes in the layer height, the model for 4.9 nm-thick aptamer layer incorporated a proportional increase of the charge density by 12%. This value stems from the height ratio between the extended *vs.* contracted aptamer molecule (5.5 *vs.* 4.9 nm). The increase in the charge density upon target recognition, manifests as an increasingly pronounced rectification, with higher current magnitudes at negative bias and slightly lower currents in the positive $I-V$ curve branch (Figure S6). Yet, there is still a negligible difference between the free *vs.* target-bound aptamer layer curves at positive voltages.

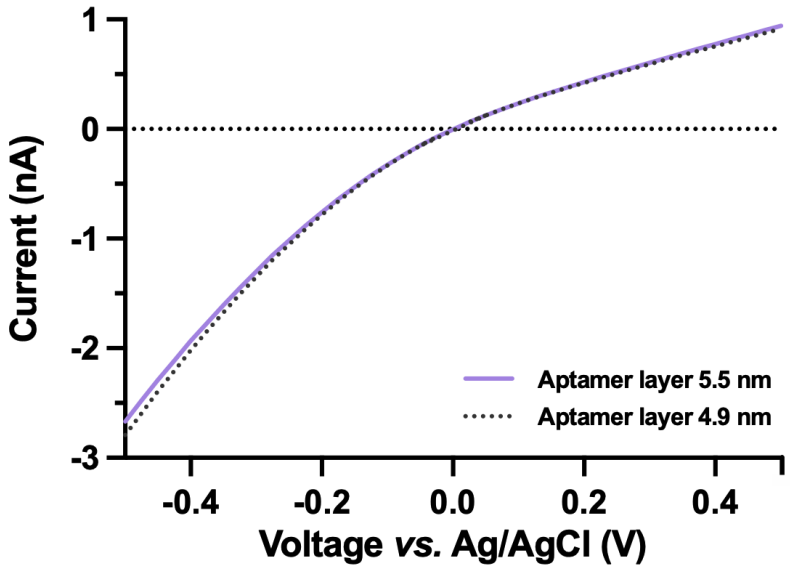

Figure. S6: Simulated $I-V$ characteristics of the nanopipettes with aptamer layer thicknesses of 5.5 (solid purple line) and 4.9 nm (dotted grey line) with concentration of fixed charges of 200 mM and 224.5 mM ((5.5 nm/4.9 nm)*200 mM) respectively.

Aptamer layer compression that incorporates ion permeability

In addition to the effect of charge density changes upon target capture, the change of ion permeability through the aptamer layer was also introduced into the model by varying the factor f from 1 to 4.9 nm/5.5 nm = 0.891. Changing this value affects the diffusion constant D_i of all ionic species in the domain II of the model. Figure S7 shows how the ion mobility in the aptamer layer impacts the overall ionic current in the aptamer-modified nanopore. In this model, the ion current magnitude is visibly smaller at positive biases upon compressing the aptamer layer and lowering the ion mobility (solid purple curve *vs.* red dashed curve). Negligible differences are observed at negative voltages upon compressing the layer and reducing the ion mobility as the effects of altered ion mobility and more compact charge have opposite effects. The overlapping effects of reduced permeability hindering ionic flux and higher density of charge increasing the flux, counteract each effect, causing a less pronounced ion current change.

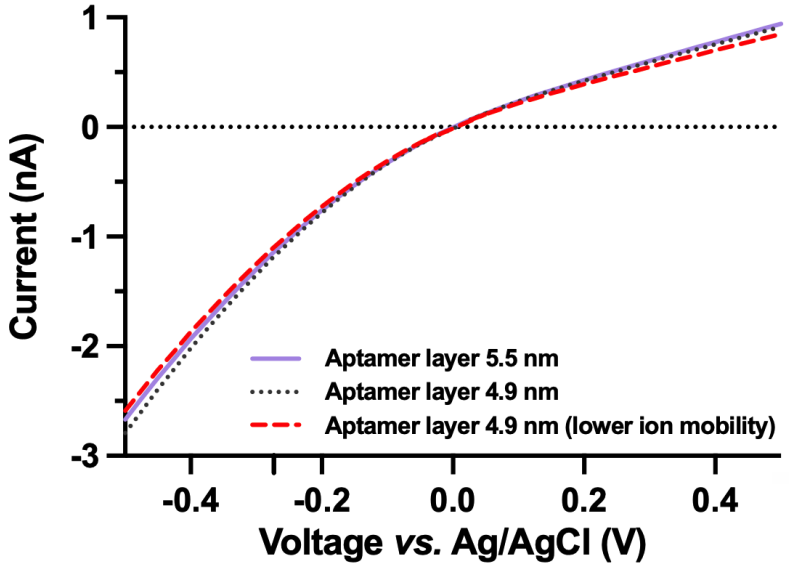

Figure. S7: Simulated $I-V$ characteristics of the nanopipettes with aptamer layer thickness of 5.5 (solid purple line) and 4.9 nm (dotted grey line), with concentration of fixed charges of 200 mM and 5.5/4.9 * 200 mM = 224.5 mM, respectively. The dashed red line reveals ion currents simulated for the contracted aptamer layer with proportionally reduced ion mobility.

SI-4. Dukhin number calculation

The Dukhin number (Du) was approximated to compare the ratio of ionic flux occurring along the nanopipette walls *vs.* through the center of the nanopipette:[4]

$$Du = (|\sigma|/e)/c * R \tag{5}$$

Where e represents the elementary charge and c the ionic bulk concentration at 150 mM, corresponding to the salt content of 1x PBS. A value of 5 nm was used for the nanopore radius, R. The surface charge density, σ, was approximated by projecting the number of negative charges associated with one aptamer (44 negative charges per sequence), onto the surface required for the unbound state of an aptamer; the lower rectangular surface from the tightest fitting box, extracted from the MDS of the respective aptamer (Figure 4).

Our approximations result in a Dukhin number of around 8.4 and 4.0 for the dopamine and serotonin aptamers tethered within a 10 nm nanopore, respectively. Both of these values imply that the contribution of the overall ionic flux originating from the flux along the nanopore wall dominate when compared to bulk flux. We note however, that the surface charge density approximation disregards the height of the aptamer, which covers a large portion of the nanoscale orifice. Therefore, a simple projection onto the wall does not necessarily represent the true wall charge of the nanopore.

SI-5. Estimation of theoretical current

To estimate the current passing through the area of the nanopore covered with DNA, the formula from Wang et al.[5] was used. Here the experimentally obtained signal, $I_{measured}$, can be described as:

$$I_{measured} = I_{open} - I_{excluded} + I_{aptamer} \tag{6}$$

I_{open}: current through the bare unmodified nanopore (value obtained experimentally).

$I_{excluded}$: current excluded due to the presence of aptamers immobilized inside the nanopore.

$I_{aptamer}$: current passing through functionalized layer of aptamers.

By utilizing the dimensions extracted from the MDS, the $I_{excluded}$ was estimated from the excluded volume:[5]

$$I_{excluded} = \frac{V}{L_{pore}}(N * area_{aptamer}(\mu_{Na} + \mu_{Cl})cN_A e) \tag{7}$$

where V is the applied voltage (500 mV), L_{pore} is the sensing length of the nanopore (simulated to be ~30 nm),[6] μ_{Na} and μ_{Cl} are the bulk mobilites of Na^+ and Cl^- ions (5.18 * 10^{-8} m^2 V^{-1} s^{-1} and 7.91 * 10^{-8} m^2 V^{-1} s^{-1}, respectively[7]), c is the molar concentration of NaCl in mol/m^3, N_A is Avogadro's number, and e is the fundamental charge.[8] The $area_{aptamer}$ represents the cross-sectional area occupied by one aptamer within the orifice. This value was calculated from the dimensions of the aptamers extracted from the MDS (dimensions are found in the main text, Figure 3, 3.95*5.46=21.56 nm^2 and 4.21*5.72=24.08 nm^2 for dopamine and serotonin aptamers, respectively). The N represents the number of aptamers within the orifice, which can be estimated as the number of aptamers capable of binding within the 10 nm diameter opening, by dividing the circumference by the dimensions of the lower rectangle from the MDS aptamer structures (Figure 3c,f).

According to equation 7, the excluded current changes upon introduction of the neurotransmitter target for both the dopamine and serotonin aptamers as the cross-sectional area of DNA through which ionic flux traverses is modified upon conformational rearrangement.

A compression of the aptamer layer, as is the case upon dopamine binding, results in a lower projected area of DNA coverage within the pore, and thus reduces the excluded current, while the inverse can be approximated for an aptamer layer elongation.

The $I_{excluded}$ values for dopamine and serotonin were calculated as relative values before and after target exposure, and opposite directionalities of current change were observed. Specifically, $I_{excluded}$ *decreased* by around 20% for dopamine and *increased* by approximately 10% for serotonin. Subsequently, $I_{aptamer}$ was obtained according to equation 6, resulting in the same exhibited directionality of behavior as $I_{excluded}$ for both dopamine and serotonin.

It is however important to note that these values, $I_{excluded}$ and $I_{aptamer}$, depend on the parameters used in equation 7, in particular, N, L_{pore}, and c. Nevertheless, fixing the same values for dopamine and serotonin, the divergent behaviour is always observed (*ie.* a decreasing current for dopamine and an increasing current for serotonin). These directional changes in ionic currents support both the experimental observations and COMSOL simulations: when the aptamer layers are compressed, a decrease in ionic flux is observed upon dopamine binding. Conversely, when the aptamer layer is elongated due to serotonin binding, an increase in ionic flux is reported.

References

(1) Vogt, B. D.; Lin, E. K.; Wu, W.-l.; White, C. C. Effect of Film Thickness on the Validity of the Sauerbrey Equation for Hydrated Polyelectrolyte Films. *The Journal of Physical Chemistry B* **2004**, *108*, 12685–12690.

(2) Vogt, B. D.; Soles, C. L.; Lee, H.-J.; Lin, E. K.; Wu, W.-l. Moisture Absorption and Absorption Kinetics in Polyelectrolyte Films: Influence of Film Thickness. *Langmuir* **2004**, *20*, 1453–1458.

(3) Nakatsuka, N.; Heard, K. J.; Faillétaz, A.; Momotenko, D.; Vörös, J.; Gage, F. H.; Vadodaria, K. C. Sensing serotonin secreted from human serotonergic neurons using aptamer-modified nanopipettes. *Mol Psychiatry* **2021**, *26*, 2753–2763.

(4) Poggioli, A. R.; Siria, A.; Bocquet, L. Beyond the Tradeoff: Dynamic Selectivity in Ionic Transport and Current Rectification. *J. Phys. Chem. B* **2019**, *123*, 1171–1185.

(5) Wang, V.; Ermann, N.; Keyser, U. F. Current enhancement in solid-state nanopores depends on three-dimensional DNA structure. *Nano Letters* **2019**, *19*, 5661–5666.

(6) Nakatsuka, N.; Faillétaz, A.; Eggemann, D.; Forró, C.; Vörös, J.; Momotenko, D. Aptamer Conformational Change Enables Serotonin Biosensing with Nanopipettes. *Analytical Chemistry* **2021**, *93*, 4033–4041.

(7) Smeets, R. M.; Keyser, U. F.; Krapf, D.; Wu, M.-Y.; Dekker, N. H.; Dekker, C. Salt dependence of ion transport and DNA translocation through solid-state nanopores. *Nano letters* **2006**, *6*, 89–95.

(8) Hille, B. *Ion Channels of Excitable Membranes; Sinauer*; Sunderland, 2001.